

## Fireball and Shock Wave Dynamics in the Detonation of Aluminized Novel Munitions

J. M. Gordon<sup>a</sup>, K. C. Gross<sup>a</sup>, and G. P. Perram<sup>a</sup>

UDC 6.011+533.231.4

Translated from *Fizika Goreniya i Vzryva*, Vol. 49, No. 4, pp. 76–90, July–August, 2013.  
Original article submitted April 10, 2012.

**Abstract:** High-speed 4-kHz visible imagery from 13 field detonations of aluminized RDX munitions with varying liner compositions are collected to study shock wave and fireball dynamics. The Sedov–Taylor point blast model is fitted to shock front temporal history data, and blast wave characteristics are interpreted by varying the energy release factor  $s$  and blast dimensionality  $n$ . Assuming a constant rate of energy release ( $s = 1$ ), the Sedov–Taylor model establishes a near-spherical expansion with the dimension  $n = 2.2$ – $3.1$  and shock energies of 0.5–8.9 MJ. These shock energies correspond to efficiencies of 2–15% of the RDX heats of detonation. A drag model for the fireball size yields a maximum radius of  $\approx 5$  m, which is consistent with the luminous fireball size in visible imagery, and initial shock speeds corresponding to Mach numbers of 4.7–8.2. Initial shock speeds are smaller than the RDX theoretical maximum speed by a factor of 3–4. Shock energy decreases if aluminum is in the liner rather than in the high explosive.

**Keywords:** shock waves, fireball, classification, detonation, aluminized RDX, Sedov–Taylor point blast model.

**DOI:** 10.1134/S0010508213040084

### INTRODUCTION

The classification of battlespace combustion events from visible and infrared signatures requires new field data, simplified phenomenological models, and the correlation of key features with event characteristics. Despite the inherent variability in radiant intensity of post-detonation fireballs, we have demonstrated a connection between mid-infrared spectral signatures associated with H<sub>2</sub>O and CO<sub>2</sub> combustion products and the stoichiometry of significantly different high explosive (HE) materials [1]. More recently, a suite of radiometers, imagers, and spectrometers was deployed to collect signatures from RDX-based explosives with variations only in the aluminum content and liner composition [2]. We hope to extend the classification to these additional events by developing correlations between spectral features and imagery signatures. In particular, the evolu-

ing temperature of the post-detonation combustion fireball might be related to detonation shock wave dynamics since a higher detonation efficiency may suggest less material available in the afterburn phase of the explosion event.

The shock wave analysis is found in a multitude of applications ranging from pulsed laser deposition to bomb detonations to astrophysical events. Cox [3] and Raymond [4] applied the shock analysis to interstellar phenomena by modeling a gas as it interacts with a shock front from a supernova remnant. Astrophysical time scales enable the presumption of a steady-state flow of similarly affected gases, thus, allowing temporal integration of the spectrum instead of spatial integration. Dokuchaev [5] analytically derived the behavior of a time-dependent spherical shock wave in astrophysical scales by assuming the shock wave to be continuously pumped or injected by a constant-luminosity central source through some radiative mechanism. For the present work, methodologies and techniques from pulsed laser ablation [6–9] and bomb explosion analyses [10–12] are used.

<sup>a</sup>Department of Engineering Physics, Air Force Institute of Technology, 2950 Hobson Way, Wright-Patterson Air Force Base, Ohio, USA; glen.perram@afit.edu.

By monitoring the strength and propagation speed of detonation shock waves, the energy released in the explosive event can be inferred using blast wave models [6–12]. The remaining energy from the heat of detonation may be available for secondary combustion driving the fireball temperature dynamics.

Shock wave propagation, the size of the emissive fireball, and the maximum extent of detonation products evolve differently, and the characterization of the detachment of the shock front from the fireball is not well captured in simplified empirical models [13–16]. Dispersal of particulate materials is likely controlled by the initial velocity and subsequent drag [10]. One might anticipate that the initial velocity matches the shock propagation, but the effective drag coefficient and the maximum extent of the fireball are harder to predict. The correlation of the fireball size as determined from imagery and spectra may depend on the spectral band and is poorly understood [1, 17]. The present work characterizes the visible fireball size and shock propagation.

The effect of the aluminum content in condensed high explosives (HEs) has been studied in some detail [14, 18–23]. However, the precise influence of aluminum on shock dynamics is not completely understood. Studies show that its influence is limited to short time scales, preferably in the presence of oxygen, if it is to support propagation of the shock front due to the liberation of chemical energy during the reaction [21]. Gilev and Anisichkin [23] used electrical conductivity measurements during an explosion to suggest that the reaction of aluminum with detonation products occurs within a microsecond time span immediately upon detonation. Analyzing the solid residue after a detonation in an explosion chamber, they concluded that a thin oxide layer quickly formed around the aluminum particles effectively inhibits a further reaction of bulk aluminum with other species, resulting in the majority of the aluminum additive acting as inert non-participants in the detonation. They further concluded that the thermal energy contribution from the reaction between the aluminum additives and detonation products in their tests [23] was 5–14% of the overall HE energy. Their tests also showed that a smaller aluminum particle size resulted in a larger fraction of reacted aluminum. Lefrancois et al. in their work on the effect of nanometric aluminum additives to HEs [20] suggested that particles of the order of 100 nm in size do not add to the ballistics performance of aluminized RDX-based HEs. They attributed this fact to the presence of a thin (3 nm) layer of  $\text{Al}_2\text{O}_3$  on the surface of the aluminum particles. However, they found that reflected blast waves and reflected impulse are strengthened by these metallic nanoscale additives. They attributed these results to

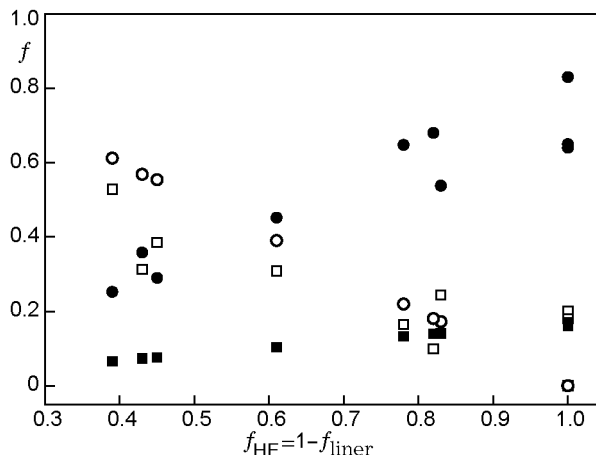


**Fig. 1.** Weight fractions of various species for different HE weight fractions: liner ( $\circ$ ), aluminum in both the liner and HE ( $\square$ ), RDX ( $\bullet$ ), and binder ( $\blacksquare$ ).

the long-time thermal transfer from hot aluminum particles to gaseous detonation products occurring during hundreds of microseconds to a few milliseconds. Other studies [22, 24] suggested the performance benefits of aluminum may lie in time scales well beyond the detonation. The impact of aluminum on the size of the emissive fireball is largely unexplored [25, 26].

## 1. EXPERIMENTAL

Thirteen aluminized novel munitions varying in the HE content from 6.3 to 16.9 kg and liners of 2.8–10.7 kg were detonated at the Air Force Research Laboratory’s Advanced Warhead Experimentation Facility (AWEF) in Florida, U.S.A. The test article was centered within concentric rings of instrumented pressure probes arranged at 3.05 m increments from the center. The presence of the tree line behind the test arena was fortuitous for shock front tracking because it provided good contrast during digital image processing.

The test article consists of a cylindrical tube of mild steel with an inner and outer diameters of 17.8 cm and 20.3 cm, respectively. The test article is filled with an aluminized RDX-based HE or a combination of this explosive and a reactive liner in varying amounts according to Table 1. The events in Table 1 and subsequent tables are listed from the most to least amount of the HE weight in the test articles. The event nomenclature (E) denotes the chronological order in the test sequence. For cased explosives with the length-to-diameter ratio  $L/D > 2$ , the work function associated with the strength of damage done by the pressure at the end of the charge approaches a constant value [27].

**Table 1.** Composition of test articles

Event	HE			Liner			Total munition		Weight fraction				
	weight, kg	RDX, kg	Al, kg	weight, kg	volume, %	Al, kg	weight, kg	Al, kg	liner	RDX	HE	binder	Al
E13	16.92	10.83	3.38	0	0	0	16.92	3.38	0	0.64	1.00	0.16	0.20
E5	16.74	10.88	3.01	0	0	0	16.74	3.01	0	0.65	1.00	0.17	0.18
E10	15.84	13.14	0	0	0	0	15.84	0	0	0.83	1.00	0.17	0
E8	15.83	13.14	0	0	0	0	15.83	0	0	0.83	1.00	0.17	0
E4	13.42	8.72	2.42	2.78	20	1.53	16.20	3.95	0.17	0.54	0.83	0.14	0.24
E17	13.37	8.69	2.41	2.78	20	1.53	16.15	3.94	0.17	0.54	0.83	0.14	0.24
E12	12.69	10.53	0	3.56	20	2.67	16.25	2.67	0.22	0.65	0.78	0.13	0.16
E16	12.67	10.52	0	3.56	20	2.67	16.24	2.67	0.22	0.65	0.78	0.13	0.16
E7	12.65	10.50	0	2.78	20	1.53	15.43	1.53	0.18	0.68	0.82	0.14	0.10
E11	9.75	7.21	0.88	6.23	40	4.05	15.98	4.93	0.39	0.45	0.61	0.10	0.31
E6	6.75	4.39	1.22	10.65	60	7.99	17.40	9.20	0.61	0.25	0.39	0.07	0.53
E15	6.69	4.35	1.20	8.33	60	4.58	15.02	5.78	0.55	0.29	0.45	0.08	0.39
E3	6.31	5.24	0	8.33	60	4.58	14.64	4.58	0.57	0.36	0.43	0.07	0.31

## 2. IMAGE PROCESSING

The total device weight is nearly constant, so that the fraction of the weight allocated to the liner and aluminum decreases as the HE weight increases (Fig. 1). The average aluminum particle size is  $23\ \mu\text{m}$ . The test articles without liners are coated with a very thin layer (0.1 mm) of an asphaltic hot-melt to prevent contact between the metal casing and the HE. The test article is capped at the bottom with a 1.27-cm steel plate bolted to the cylinder and capped at the top with a detonation train consisting of the RP-80 exploding bridge wire, A-5 booster (diameter 2.54 cm, thickness 2.54 cm, and weight  $\approx 110$  g), Comp-B booster (diameter 5 cm, thickness 5 cm, weight  $\approx 120$  g), and Comp-B booster (diameter 20 cm, thickness 2.52 cm, weight  $\approx 1.5$  kg).

A suite of instruments consisting of a four-band radiometer, an FTIR spectrometer, an audio-visual witness camera, and Phantom v5.1 and v7.1 high-speed digital cameras collected signatures from an unobstructed standoff distance of 335 m. For the present research, 8-bit gray-scale,  $768 \times 384$  pixel visible signatures from the Phantom v5.1 were used as the primary data set. The images were collected at 3000 and 4200 frames per second (fps) with an effective horizontal field-of-view (FOV) of about 70 m or 91 cm/pixel. The exposure times ranged from 50 to 240  $\mu\text{s}$  to prevent saturation and produce well-contrasted gray-scale images. Meteorological conditions for all tests were monitored.

A single image from event E8 at 13 ms after detonation is illustrated in Fig. 2a. The fireball and the particulate cloud expand to a radius of about 5.6 m. In this frame, the image is dominated by dark soot with a small bright region representing post-detonation combustion. High-speed fragments intercepting the dirt just outside the fireball volume can also be seen. Tracking of the shock wave front is made possible by frame-differencing images that are 3–5 frames apart [28]. Figure 2b illustrates this difference on a logarithmic scale. The shock wave front and the secondary reflected shock are readily observed. The displacement of the shock front from the detonation origin ( $R_s$ ) is determined to within about 1 pixel at a temporal resolution of 0.24–0.33 ms. The shock front is nearly hemispherical, with a width-to-height ellipticity  $\varepsilon = 0.95$ . The location of the shock front is tracked along an angle of  $\approx 15^\circ$  relative to the ground. This line of observation was chosen as it provided the best-contrasted images for the greatest number of image frames. As it will be discussed in Section 3.1, the ground effects do not influence the behavior of the shock front dimensionality along this line of observation. The detonation point of origin is defined as the center of the steel test article.

Figure 2c highlights the emissive pixels of the fireball (gray) and the pixels with soot (black), illustrating the maximum extent of the fireball. The shock front is well detached from the emissive fireball and soot cloud

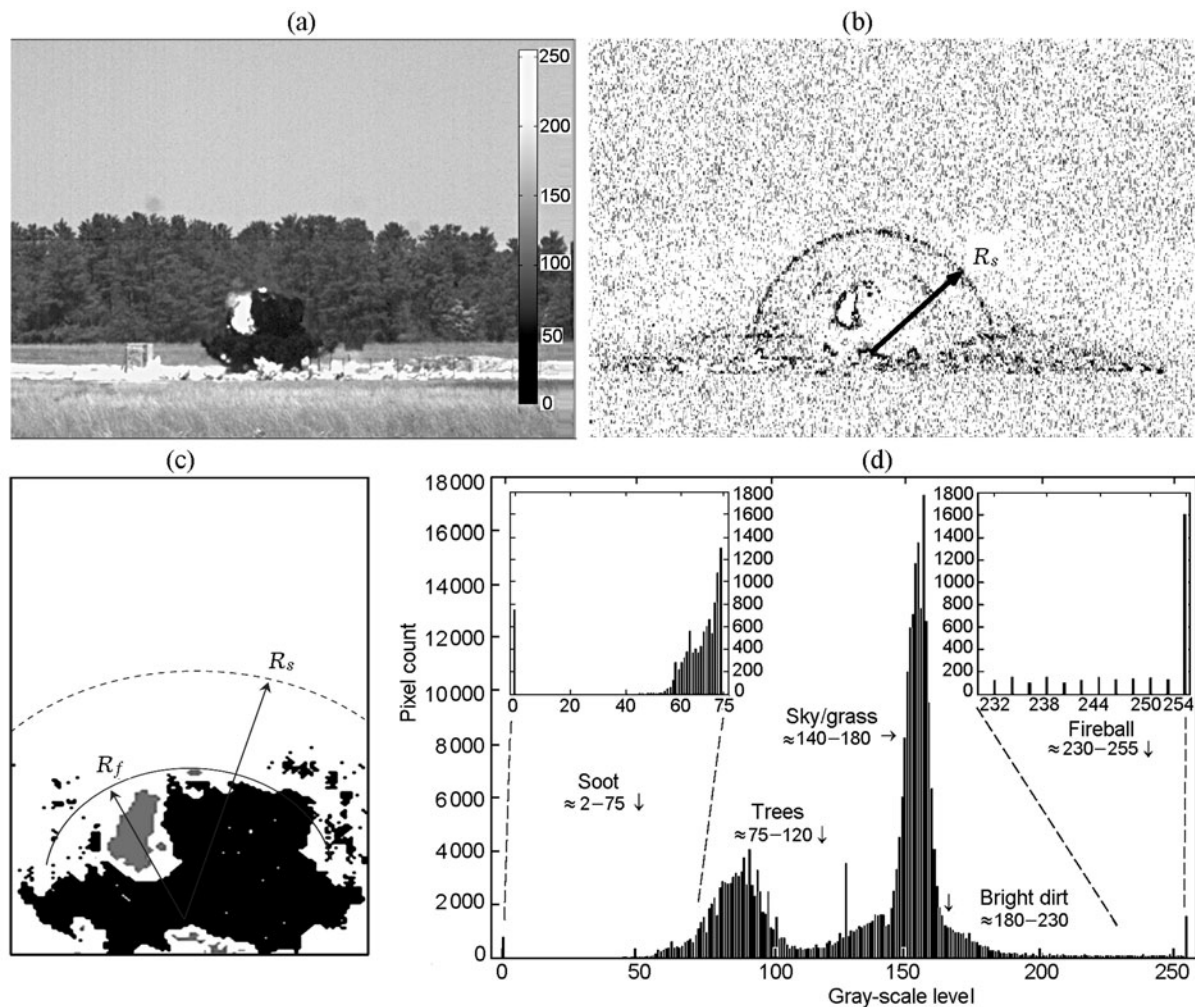


**Fig. 2.** Visible image for event E8 at the time  $t = 13$  ms after detonation: (a) image with the 8-bit gray scale for intensity; (b) image processed by taking the  $\log_{10}$  of the frame-differenced image; (c) intense pixels of the fireball of radius  $R_f$  (gray) and dark pixels of soot (black); (d) histogram of the image showing the 8-bit number range of gray-scale pixel intensity levels of various features.

at  $t = 13$  ms after detonation. The shock wave propagates to  $R_s = 10.1$  m, well beyond the maximum extent of the fireball,  $R_f = 5.6$  m. Figure 2d depicts a histogram of the 8-bit digital number gray scale of the original image. Note that the pixels of interest (fireball and soot) are located in the wings of the histogram and are easily separable from the majority of the pixels in the image constituting grass, trees, and sky. The radius of the fireball front  $R_f$  is defined as the distance from the detonation point of origin to the maximum extent of the fireball edge along an angle similar to that used to track the shock front  $R_s$ .

For each detonation event, the first 20–30 frames are individually analyzed to obtain the most accurate

tracking of the luminous fireball growth. The elapsed time is recorded by taking the difference of the embedded time stamps between successive frames. After the shock wave detaches from the fireball, only every fifth or tenth succeeding frame is analyzed for the fireball and shock wave radii.

Much later in the development of the fireball, an emissive area rises and flattens, as is shown for event E7 in Fig. 3. At  $t = 0.35$  s, the fireball size has grown to a radius of more than 6.1 m and risen to a height exceeding 13 m. The ellipticity for the post-detonation particulate cloud (PDPC) or plume cloud at  $t = 0.35$  s is  $\varepsilon = 0.72$ , compared to the shock wave ellipticity  $\varepsilon = 0.95$  at  $t = 0.01$  s.

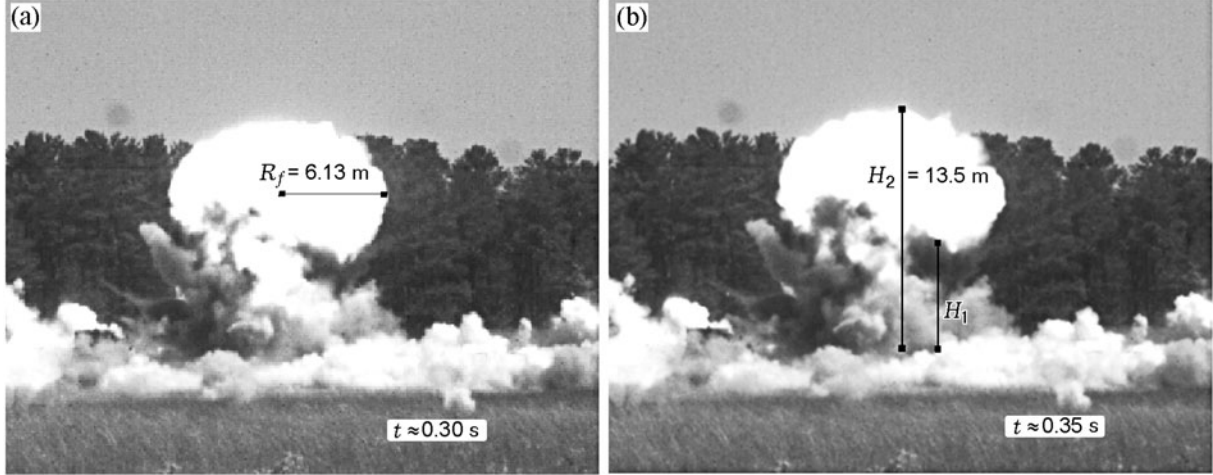


**Fig. 3.** Fireball from event E7:  $H_1$  is the height of the bottom of the PDPC plume;  $H_2$  is the fireball lofting height measured from the blast origin to the top of the PDPC plume.

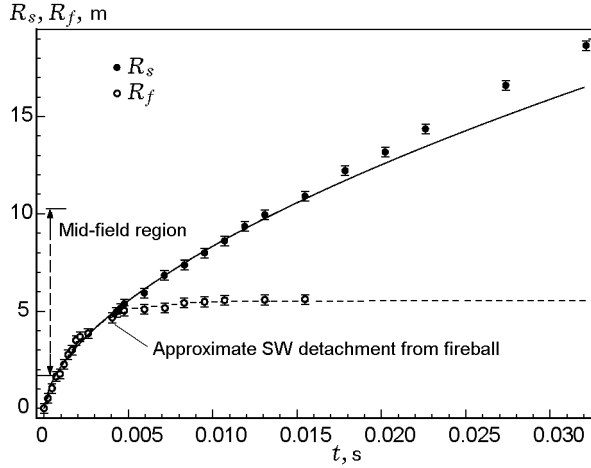


**Fig. 4.** Fit of the blast model (solid curve) and exponential drag model (dotted curve) of the experimental values of the shock front radius  $R_s$  and fireball radius  $R_f$  in event E7: the Sedov–Taylor blast theory is valid in the mid-field region.

### 3. RESULTS AND DISCUSSION

The shock wave analysis is accomplished using the Sedov–Taylor model where the blast dimensionality, the rate of energy release, and the blast energy can be examined. The fireball size dynamics resulting from post-detonation combustion is analyzed by using a drag model.

#### 3.1. Shock Wave Analysis

The radii of the shock front  $R_s$  and fireball  $R_f$  for event E7 are illustrated as functions of time in Fig. 4.

The shock front detaches from the fireball at about 4 ms. The fireball reaches the maximum radius of about 5 m shortly after detachment. The shock wave approaches a constant speed close to the speed of sound at  $t = 30$  ms (the Mach number is  $M = 1.06$ ).

The Sedov–Taylor blast model [10, 11] is used to characterize the shock wave propagation

$$R_s(t) = at^b, \quad (1)$$

$$b = (s + 2)/(n + 2), \quad (2)$$

where  $n$  is the expansion dimensionality: planar expansion ( $n = 1$ ), cylindrical expansion ( $n = 2$ ), and spherical expansion ( $n = 3$ );  $s$  is the factor characterizing the rate of energy release: instantaneous energy release ( $s = 0$ ) and constant-rate energy release ( $s = 1$ ). The coefficient  $a$  of the energy released in the detonation  $E_d$  is characterized via a length scale  $l_0$ , a time scale  $\tau_0$ , and the atmospheric mass density  $\rho$  as [10, 29, 30]

$$a = \left( \frac{E_d / (\tau_0^s l_0^{3-n})}{\rho} \right)^{1/(n+2)}. \quad (3)$$

For  $n = 3$  and  $s = 0$ , the length and time scales do not contribute to the interpretation of the energy released. For  $n = 3$  and  $s = 1$ , the factor  $E_d/\tau_0$  may be interpreted as the rate of energy release.

The applicability of the Sedov–Taylor expression is limited to the mid-field region, where the shock wave has expanded to displace a mass of air exceeding the HE mass  $m$ , but the pressure differential across the shock is still significant as compared to the ambient background pressure  $p$  [8]. All these features are described by the equation

$$\left( \frac{3m}{2\pi\rho} \right)^{1/3} \ll R_s \ll \left( \frac{\Delta H_d}{p} \right)^{1/3}. \quad (4)$$

**Table 2.** Scales

Event	Scales	
	$l_0$ , m	$\tau_0$ , ms
E13	1.25	0.14
E5	1.24	0.14
E10	1.32	0.15
E8	1.32	0.15
E4	1.13	0.13
E17	1.16	0.13
E12	1.21	0.14
E16	1.22	0.14
E7	1.21	0.14
E11	1.09	0.12
E6	0.90	0.10
E15	0.91	0.10
E3	0.96	0.11

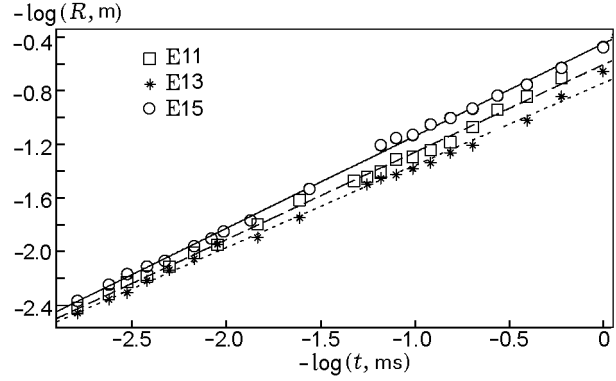
At early times immediately after detonation and before shock wave detachment, the fireball front in the mid-field region is used to represent the shock wave front during the Sedov–Taylor blast model fit. A wave reflected from the ground can produce a stronger Mach wave when combined with the initial shock wave [31, p. 13]. The test articles in the present work are sufficiently elevated above the ground surface, so that the ground-reflected shock front has not yet combined with the initial shock during the temporal regime that the Sedov–Taylor blast model is fitted to the shock front data. Examination of high-speed visible imagery confirms that only the initial shock wave front is modeled by the Sedov–Taylor model in the mid-field region. From Eq. (3), the length scale necessary for proper interpretation of the energy may be defined as the beginning of the mid-field region:

$$l_0 = \left( \frac{3m}{2\pi\rho} \right)^{1/3}. \quad (5)$$

The use of other length scales, such as the device length or device diameter, results in low derived detonation energies  $E_d$ . The corresponding time necessary to reach the mid-field region  $\tau_0$  is determined by the formula [27]

$$\tau_0 = l_0/v_{\text{RDX}}, \quad (6)$$

where  $v_{\text{RDX}} = 8.8$  km/s is the ideal detonation wave velocity for RDX at the theoretical maximum density  $\rho_{\text{max}}^{\text{calc}}$ . At  $\rho_{\text{max}}^{\text{calc}} = 1.81$  g/cm<sup>3</sup>, the RDX detonation wave traveling at 8.8 km/s can traverse the length of

**Fig. 5.** Log-log plot of shock expansion and two-parameter power law fit showing the relative spread of the blast model fits for  $t = 0$ –20 ms.

the 0.4064-m test article in about 46.2  $\mu$ s. The corresponding length and time scales for each event are provided in Table 2. Figure 4 illustrates the mid-field region for event E7 extending from 1.2 to 10.2 m. The camera captures the expansion well before and after the mid-field region. The shock detaches from the fireball about half-way through the mid-field region.

A fit of Eq. (1) to the observed shock expansion for event E7 is illustrated in Fig. 4. Equation (1) is fitted only to the data points in the mid-field region. The transition to a sonic shock ( $M = 1$ ) in the far-field region is not well captured by the Sedov–Taylor model. The resulting fit parameters,  $a$  and  $b$ , and their associated uncertainties,  $\delta a$  and  $\delta b$ , for each event are reported in Table 3. The uncertainties are defined as half of the difference between the upper and lower intervals of the 95% confidence bounds of the fit. Sedov–Taylor model fits are also reported for the case where the exponent is constrained to  $b = 0.6$  (the case with  $n = 3$  and  $s = 1$ ). Table 3 also lists the fit parameters and uncertainties of the drag model [Eq. (9) in Section 3.3].

A log-log plot of shock expansion for several events is provided in Fig. 5. The small, but readily discernible variations in intercepts and slopes correspond to variations in the two fit parameters. The trend in these slopes and intercepts with munitions characteristics, particularly the weight fractions is analyzed in the present work.

The two fit parameters  $a$  and  $b$  are insufficient to fully determine the dimensionality  $n$ , the rate of energy release  $s$ , and the energy released  $E_d$ . Several cases for interpreting the dimensionality of shock expansion and the energy release constants are provided in Table 4. The case where the exponent is constrained to  $b = 0.6$  yields detonation energies of 2.4–8.8 MJ. These solutions are constrained to  $s = 1$  corresponding to the

**Table 3.** Fit parameters for shock expansion and fireball drag

Event	Sedov–Taylor model, $b = 0.6$		Sedov–Taylor model					Drag model				
	$a$	$\delta a$	$a$	$\delta a$	$b$	$\delta b$	RMSE	$R_m$ , m	$\delta R_m$ , m	$k$ , s <sup>-1</sup>	$\delta k$ , s <sup>-1</sup>	RMSE
E13	136	1	144	11	0.611	0.017	0.145	5.76	0.13	426	20	0.049
E5	138	3	159	19	0.631	0.025	0.185	4.90	0.12	527	38	0.122
E10	133	1	132	8	0.599	0.012	0.074	4.54	0.07	609	27	0.077
E8	136	2	135	26	0.599	0.037	0.198	5.57	0.13	422	27	0.121
E4	134	1	137	15	0.604	0.023	0.177	5.05	0.15	500	52	0.204
E17	136	2	156	15	0.629	0.020	0.183	5.31	0.11	455	27	0.128
E12	132	2	153	18	0.630	0.025	0.226	5.07	0.11	509	34	0.142
E16	134	4	188	12	0.674	0.014	0.138	5.08	0.08	431	20	0.096
E7	132	2	125	18	0.588	0.029	0.190	5.53	0.10	470	27	0.115
E11	130	2	165	9	0.651	0.012	0.107	5.66	0.15	360	26	0.172
E6	125	3	186	15	0.689	0.019	0.198	5.15	0.22	374	42	0.227
E15	122	3	186	12	0.693	0.014	0.114	4.31	0.24	457	39	0.143
E3	111	2	189	21	0.712	0.023	0.168	4.81	0.24	327	30	0.032

Note: RMSE is the root-mean-square error.

**Table 4.** Interpretation of shock dynamics

Event	$s = 1, n = 3$			$s = 0$		$s = 1$					$n = 3$			Calculation of $\Delta H_d$	
	$dE_d/dt$ , GW	$E_d$ , MJ	$\tau_{\text{RDX}}$ , ms	$E_d$ , MJ	$n$	$dE_d/dt$ , GW	$E_d$ , MJ	$\tau_{\text{RDX}}$ , ms	$\eta$	$n$	$E_d$ , MJ	$\eta$	$s$	RDX, MJ	HE, MJ
E13	57.05	8.07	1.07	20.41	1.27	48.28	6.83	1.26	0.11	2.91	9.46	0.16	1.06	60.99	126.59
E5	60.98	8.59	1.01	17.68	1.17	39.01	5.49	1.57	0.09	2.76	13.30	0.22	1.15	61.30	130.54
E10	51.37	7.68	1.44	23.79	1.34	52.20	7.80	1.42	0.11	3.01	7.47	0.10	0.99	74.05	138.28
E8	58.72	8.79	1.26	25.98	1.34	59.51	8.91	1.24	0.12	3.01	8.60	0.12	0.99	74.03	138.14
E4	57.40	7.38	0.86	19.12	1.31	53.69	6.90	0.92	0.14	2.97	7.76	0.16	1.02	49.14	104.59
E17	54.85	7.25	0.89	14.86	1.18	35.88	4.74	1.36	0.10	2.77	10.91	0.22	1.14	48.96	104.19
E12	52.54	7.22	1.13	15.75	1.17	34.16	4.70	1.74	0.08	2.76	11.10	0.19	1.15	59.33	110.80
E16	55.27	7.64	1.07	10.68	0.97	18.99	2.62	3.12	0.04	2.45	19.89	0.34	1.37	59.26	110.62
E7	52.55	7.22	1.13	23.71	1.40	63.27	8.69	0.93	0.15	3.10	6.06	0.10	0.94	59.15	110.40
E11	45.34	5.60	0.90	9.26	1.07	20.74	2.56	1.96	0.06	2.61	10.68	0.26	1.25	40.63	80.60
E6	38.77	3.98	0.64	4.01	0.90	9.13	0.94	2.71	0.04	2.35	10.59	0.43	1.45	24.71	52.60
E15	33.61	3.46	0.73	3.69	0.89	8.05	0.83	3.04	0.03	2.33	10.14	0.41	1.46	24.50	52.18
E3	22.37	2.43	1.32	2.93	0.81	4.93	0.54	5.98	0.02	2.21	9.85	0.33	1.56	29.51	55.14

rates of energy release of 22.4–61.0 GW, assuming the theoretical RDX detonation velocities and time scales of 0.11–0.15 ms (see Table 2). However, one would expect a considerably greater energy release under ideal conditions corresponding to the theoretical heats of detonation reported in Table 4 as 24.5–74.1 MJ. One method of characterizing the efficiency would be to define a new time scale where the detonation energy is released over a longer period:

$$\tau_{\text{RDX}} = \frac{\Delta H_{\text{dRDX}}}{dE_d/dt}. \quad (7)$$

Given  $\Delta H_{\text{dRDX}}$  in Eq. (7), a large value of  $\tau_{\text{RDX}}$  suggests that the rate of energy release ( $dE_d/dt$ ) is small. Describing the efficiency in terms of the time scale is thus reasonable since it is related to the rate of energy release in the detonation. The values of 0.64–1.44 ms for this time scale are considerably greater than the ideal RDX detonation time scales of 0.10–0.15 ms. The efficiency can thus be defined by using a ratio of energies or a ratio of time scales:

$$\eta = \frac{E_d}{\Delta H_{\text{dRDX}}} = \frac{\tau_0}{\tau_{\text{RDX}}}. \quad (8)$$

It is worth noting presently that the 100% efficiency or complete conversion of the theoretical heat of detonation into a blast wave is not possible. The detonation energy is partitioned into several processes, which reduces the amount of energy available for blast wave production. For cased charges, fragmenting the steel case, accelerating the case fragments, radiating photons, and heating the detonation products are examples of processes that can channel the detonation energy away from blast wave production. The RDX detonation pressure is roughly two orders of magnitude greater than the case strength for a typical steel case. For the mild steel case in the present work, it is reasonable to assume that less than 1% of the detonation energy is required to rupture the steel casing material [32]. The test articles in the present work are considered moderate to heavily cased charges because the 27.2-kg steel case in the present work gives case-to-charge mass ratios that range from 1.6 to 4.

A case-to-charge mass ratio in this range could result in the casing fragment kinetic energy that is about 50% of the detonation energy [32]. In other words, up to about half of the detonation energy could be used in propelling the case fragments. Less than 1% of the detonation energy is lost in the form of thermal and visible radiation [32]. The remainder of the detonation energy is available to generate a blast wave. The detonation efficiencies resulting from this work may be under-estimating the actual efficiencies as we have not taken into account the precise energy losses due to the

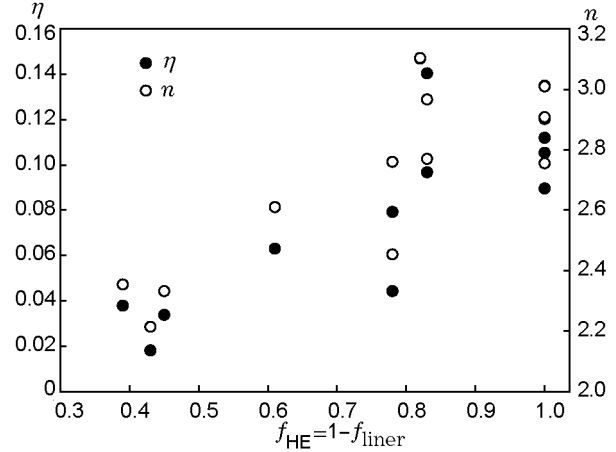


**Fig. 6.** Dependence of the shock parameters (energy efficiency  $\eta$  and dimensionality  $n$ ) on the HE weight fraction at a constant energy release ( $s = 1$ ).

casing fragment kinetic energy and thermal heating of the product gases.

The uncertainty in the parameter  $b$  is rather small, about 5% or  $\Delta b \approx 0.02$ , but the variation of  $b$  across all events is considerably larger  $b = 0.59$ – $0.71$ . Furthermore, the exponent systematically increases as the HE weight decreases. Thus, the constraint  $b = 0.6$  is not justified by the data. In an ideal point blast,  $b = 0.4$  ( $s = 0$  and  $n = 3$ ). However, we observed  $b = 0.59$ – $0.71$  ( $\pm 0.02$ ), indicating the blast dimensionality  $n < 3$  or non-instantaneous energy release  $s > 0$ . Misra and Thareja [8] reported the values for  $b$  ranging from 0.33 to 0.90 in laser-generated shock waves. They observed that  $b$  decreases as the initial energy increases and that  $b$  also decreases if the ambient atmospheric pressure is increased. In the present study, we did observe a similar decrease in  $b$  as the calculated theoretical heat of detonation increased.

For instantaneous energy release ( $s = 0$ ) the fit parameters yield the dimensionality  $n = 0.81$ – $1.40$  (i.e., somewhere between that of the planar and cylindrical geometry). However, the observed images appear nearly hemispherical. Furthermore, with this interpretation, the estimated detonation energies approach 40% of the RDX heat of detonation. Previous studies provided detonation efficiencies of 12–85% [8, 10–11, 29, 33–36] depending on test conditions. The most efficient cases involve laser ablation with a time-dependent delivery of initial energy, such as a rising laser pulse [36] or an ideal point blast in the ambient air atmosphere with a ratio of specific heats equal to 1.4 [10]. The limit of instantaneous energy release with a corresponding cylindrical dimensionality appears inconsistent with physical interpretation of the fit parameters.



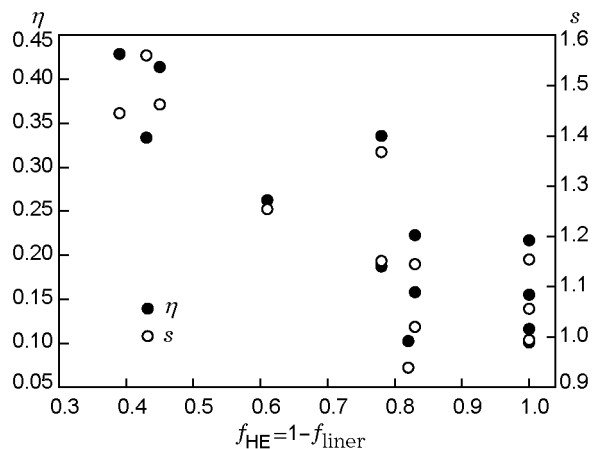


**Fig. 7.** Dependence of shock parameters (energy efficiency  $\eta$  and energy release factor  $s$ ) on the HE weight fraction at spherical expansion ( $n = 3$ ).

At  $n = 3$  (spherical shock wave), the energy release factor is  $s = 0.94\text{--}1.56$  with a mean and standard deviation of 1.22 and 0.20, respectively, and the detonation energy ranges within  $E_d = 7.7\text{--}19.9$  MJ. However, the detonation energy does not trend with the HE amount present (see Section 3.2), thus, making the  $n = 3$  condition doubtful. For a constant energy release ( $s = 1$ ), the dimensionality becomes more spherical:  $n = 2.21\text{--}3.10$  with a mean and standard deviation of 2.68 and 0.28, respectively. We do anticipate a value of  $n \leq 3$ , due to ground interactions and hemispherical expansion. Clearly, the present data are best described by a solution where  $n \cong 3$  and  $s \cong 1$ . At  $s = 1$ , Table 4 provides the rates of energy release ranging from 4.9 to 63.3 GW, corresponding to detonation energies of 0.54–8.9 MJ. The time scales for energy release from Eq. (7) are longer ( $\tau_{\text{RDX}} = 0.92\text{--}5.98$  ms) than those defined by the RDX detonation velocity at  $\rho_{\text{max}}^{\text{calc}}$ , namely,  $\tau_0 = 0.11\text{--}0.15$  ms. At  $s = 1$ , this is consistent with the efficiencies  $\eta = 2\text{--}15\%$ .

### 3.2. Influence of the Liner and Aluminum on Detonation Energy

The interpretation of the shock dynamics depends critically upon the assumptions regarding the expansion dimensionality. The efficiency  $\eta$  and dimensionality  $n$  derived from the Sedov–Taylor model assuming a constant rate of energy release ( $s = 1$ ) increases significantly as the fraction of the test article’s weight allocated to the HE increases (Fig. 6). Event E3 with only 43% of the weight allocated to the HE (36% RDX) exhibits a very low energy released during detonation ( $E_d = 0.54$  MJ) relative to the RDX heat of detonation

(29.5 MJ). The efficiency is low ( $\eta = 2\text{--}15\%$ ) and may reflect a rather stable composition of the munitions. In general, the efficiency increases as the HE amount increases and the fraction of the weight allocated to the liner decreases. In this view, the liner appears to contribute little to the destructive shock effects.

Alternatively, the efficiency decreases with the HE fraction if the dimensionality is constrained to  $n = 3$ . Figure 7 demonstrates larger efficiencies ( $\eta = 10\text{--}43\%$ ) when the rate of energy release is allowed to vary within  $s = 0.94\text{--}1.56$  ( $\pm 0.2$ ). Although open-air free-field detonations of conventional munitions suggest that longitudinal symmetry may exist, blast waves are not spherical for typical warheads where the overpressure and blast can vary greatly with the angle defined from the test item’s longitudinal axis [37]. Figure 7 suggests that the efficiency can be as high as 43%, yet the initial Mach speed (see Section 3.3) is lower than the peak theoretical shock speed by a factor of 3–4. Thus, we prefer a blast wave interpretation of  $s = 1$  as it is still consistent with the overall present analysis.

We can examine the influence of the liner and aluminum further by noting from Table 1 that the total weight percent of aluminum in the present test item configurations increases as the liner weight increases. There is an 88% correlation between the liner weight and the total weight percent of aluminum in the test articles. The analysis can be approached from two points of view. Analyzing the test articles using the liner weight (via its complementary fractional relation to the HE weight  $f_{\text{HE}} = 1 - f_{\text{liner}}$ ) allows a more intuitive interpretation of detonation energies and efficiencies. Our working assumption is that the HE participates fully in the detonation reaction, whereas the liner aluminum contributes mostly during the post-detonation combustion, and this interpretation appears consistent with the hypothesis put forward previously.

Subcategorizing the detonation energies using the liner volume percent may be an alternative approach. At constant energy release ( $s = 1$ ), three test articles (events E6, E15, and E3) with the highest liner volume ( $\approx 60\%$ ) produced the lowest detonation energies. This may suggest that the liner does not play a large active role in the detonation reaction. This might be because a large volume of the liner displaces a proportionate amount of the HE needed for detonation or, perhaps, the anisotropy created between the HE and the annular liner in the munition hinders the detonation. Explosive charges with no liner present generally tended to produce the highest blast wave energies. Test articles with a 20% liner volume provided the widest spread in detonation energies when the events were subcategorized by the liner volume percent.

One might anticipate that the aluminum content would contribute more to afterburning than the detonation shock. Aluminum in the HE tends to react at a later time when it burns favorably with detonation products, especially in the presence of atmospheric oxygen [24]. If aluminum reacts later, then the rate of energy release ( $dE/dt$ ) is lower, thus, resulting in a slower shock front. The heat release from aluminum might be realized later during the post-detonation combustion phase.

The influence of the aluminum content is further explored in Fig. 8. The inverse relationship between the shock energy and the total weight percent of aluminum at  $s = 1$  reinforces the notion that there is a trade-off between the HE amount and the aluminum amount in the test article. On the other hand, when the dimensionality is constrained to  $n = 3$ , the shock energy is rather independent of both the HE and overall aluminum content in the test article. As was discussed above, a purely spherical ( $n = 3$ ) interpretation of the blast dimensionality is not supported by previous field detonations of typical conventional munitions, of which the present test articles are surrogates. We thus prefer the  $s = 1$  constraint when analyzing the present work.

To further study the influence of aluminum on the efficiency, we examine those events with HE fractions of about 0.8 and 1.0 (Fig. 9). The analysis of these selected events shows no clear relationship between the overall aluminum weight fraction and the efficiency. It is possible that the distribution of the aluminum content to both the HE and liner is responsible for this lack of correlation.

### 3.3. Fireball Dynamics

The drag model [23] is chosen to study the behavior of the fireball size:

$$R_f(t) = R_m[1 - \exp(-kt)]. \quad (9)$$

Here  $R_m$  is the stopping distance and  $k$  is the drag coefficient. The observed fireball size is fit to Eq. (9) and compared to the shock wave expansion for event E7 in Fig. 4. Tracking the fireball front is a key issue to the shock wave analysis because the early fireball front and the shock wave front are coincident until shock wave detachment from the fireball. Thus, the fireball front in the mid-field region is used to represent the shock wave front in the Sedov–Taylor blast model fit at early times immediately after detonation and before shock wave detachment.

The results of the drag model fit for each event are provided in Table 3 and interpreted in Table 5. The maximum fireball radii range within 4.3–5.8 m with an

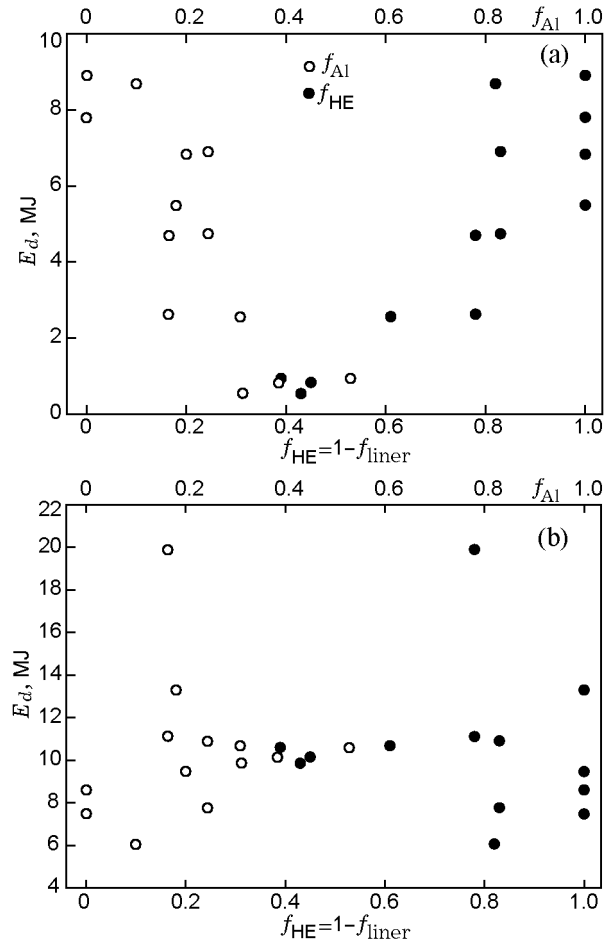


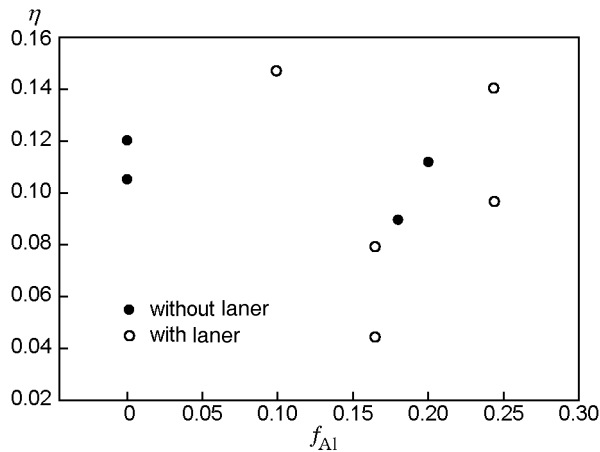
**Fig. 8.** Behavior of detonation energy with changes in the HE weight fraction  $f_{HE}$  and aluminum weight fraction  $f_{Al}$  at  $s = 1$  (a) and  $n = 3$  (b).

average of 5.1 m. An initial analysis of time-resolved infrared spectra of the same events [38] established emissive radii ranging from 3.69 to 7.17 m with an average maximum fireball emissive radius of 5.80 m. High-speed imagery indicates sooty, optically thick fireballs, suggesting emissivities close to unity. The average maximum emissive radius and the average drag model radius agree to within  $\approx 12\%$ . The fireball size quickly approaches its maximum value within 30–50 ms after initiation, with the witness camera video showing a fairly constant fireball size for 150–200 ms.

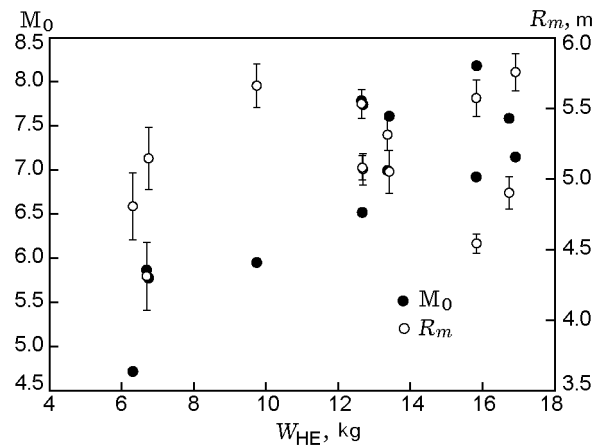
The shock wave detachment times range from 1.9 to 3.4 ms with an average detachment time of 2.7 ms corresponding to an average radial distance of  $\approx 3.7$  m from the detonation origin. A recent radiometer analysis of improvised explosive device (IED) detonations [39] suggests that the shock wave may be detaching from the luminous IED fireball at around 1.1–1.5 ms.

**Table 5.** Interpretation of fireball dynamics

Event	Initial velocity				Velocity at the near-field edge $l_0$			$H_1$ , m	$H_2$ , m	Loft velocity, m/s
	$v_0 = R_m k$ , km/s	$v_0/v_{\text{RDX}}$	$a$ , m/s	$M_0$	$t$ , ms	$R_m k e^{-kt}$ , km/s	$M$			
E13	2.45	0.28	343	7.15	0.57	1.92	5.60	11.89	14.32	11.1
E5	2.58	0.29	340	7.59	0.55	1.93	5.67	11.48	13.02	7.2
E10	2.77	0.31	338	8.18	0.56	1.96	5.81	12.38	14.75	10.9
E8	2.35	0.27	339	6.92	0.64	1.79	5.29	12.94	14.95	8.3
E4	2.53	0.29	332	7.61	0.51	1.96	5.91	11.77	14.19	11.4
E17	2.41	0.27	345	7.00	0.54	1.89	5.47	12.24	14.31	9.7
E12	2.58	0.29	333	7.74	0.54	1.96	5.89	12.73	15.27	11.9
E16	2.19	0.25	336	6.52	0.64	1.66	4.96	12.21	14.40	10.4
E7	2.60	0.30	334	7.79	0.52	2.03	6.08	12.77	14.72	9.3
E11	2.04	0.23	342	5.95	0.59	1.65	4.81	13.35	15.71	10.9
E6	1.92	0.22	333	5.78	0.52	1.59	4.76	11.98	14.35	11.3
E15	1.97	0.22	336	5.87	0.52	1.56	4.63	12.36	14.78	11.1
E3	1.57	0.18	333	4.72	0.68	1.26	3.78	11.38	13.69	10.8

**Fig. 9.** Effect of the aluminum content on the efficiency of events without the liner and with the liner constituting 17–22% by weight.

The dependences of the initial velocity and stopping distance on the HE weight are provided in Fig. 10. The detonation velocity for RDX is 8.8 km/s [27], whereas the initial detonation velocities obtained from the drag model analysis range from 1.57 to 2.77 km/s ( $M = 4.6$ –7.5). The test article initial shock velocities increase significantly with the HE weight and are about a factor of three lower in magnitude than the RDX detonation velocity  $\rho_{\text{max}}^{\text{calc}}$ . In addition to steel confinement, the presence of aluminum and wax in the HE, as well as the presence of the aluminized polyethylene annulus

**Fig. 10.** Initial velocity  $M_0$  and stopping distance  $R_m$  for the emissive fireball.

surrounding the HE, may influence the non-ideality of the detonation. As the detonation energy is defined as the sum of the kinetic energy and thermal energy in the explosion [10, 11], a factor-of-three decrease in the detonation velocity will likely result in a proportional decrease in the efficiency according to Eq. (8). This may partially explain the low energy efficiencies observed in Table 4.

At longer times ( $t \approx 0.3$  s), the fireball lofts (see Fig. 3). The fireball size remains about 4–6 m in diameter as the combustion proceeds and the fireball cools. The rate of fireball lofting approaches a constant value

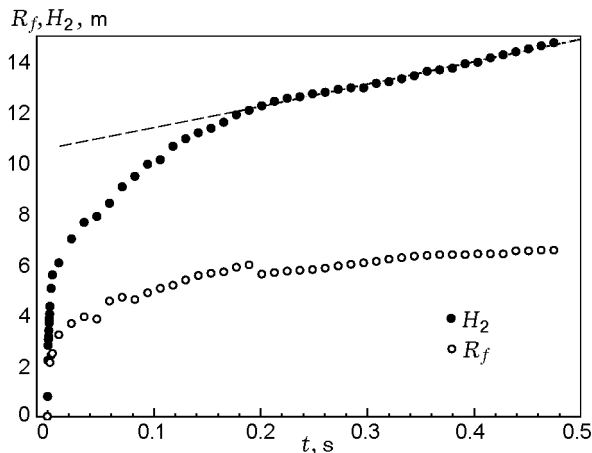


**Fig. 11.** Temporal evolution of the fireball (loft height and radius) at longer times.

at about 0.25 s (Fig. 11). This phenomenon is related to buoyancy of the fireball. These lofting rates for each event are summarized in Table 5. One would expect the lofting rates to be correlated with the fireball temperature. The temperatures can be derived from FTIR spectra recorded for these events, but radiation modeling is required, which is planned for a subsequent analysis. The lofting rates are not well correlated with the efficiencies reported in Table 4.

## CONCLUSIONS

The fireball and shock wave analysis allows the extraction of key features of the detonation event. The drag model provides a good estimate of the fireball radius (5 m) as well as shows the rapid growth of the fireball upon detonation. A subsequent study of post-detonation combustion spectra may benefit from the assumption of a rapid growth to a constant-size fireball.

The analysis of the shock wave dynamics by using the Sedov–Taylor blast wave theory is essential to estimating the shock energy and the corresponding energy conversion efficiency of the detonation. A key to the proper interpretation of the blast model energy parameter is the use of the characteristic length scale  $l_0$  and the time scale  $\tau_0$ . The initial velocity of the shock wave is directly related to the shock energy. The fit-derived initial velocity is roughly a factor of three lower in magnitude than the theoretical detonation velocity of the main HE constituent, RDX, and may help explain why the blast energies are low. The Sedov–Taylor blast model fit to data is best interpreted by using a constant energy release factor ( $s = 1$ ), occurring within the first 1–6 ms after detonation with the blast dimensionality

approaching but not equal to a spherical geometry. The HE fraction correlated with the efficiency favors the  $s = 1$  rather than the  $n = 3$  interpretation, since the positive correlation between the HE fraction and the detonation energy is more intuitive and consistent with the other findings in the analyses.

## REFERENCES

1. K. C. Gross and G. P. Perram, “The Phenomenology of High Explosive Fireballs from Fielded Spectroscopic and Imaging Sensors for Event Classification,” *Int. J. High Speed Electron. Syst.* **18** (1), 19–29 (2008).
2. J. M. Gordon, K. C. Gross, and G. P. Perram, “Temporally-Resolved Infrared Spectra from the Detonation of Advanced Munitions,” *Proc. SPIE* **7330**, 733006-1–733006-8 (2009).
3. D. B. Cox, “Theoretical Structure and Spectrum of a Shock Wave in the Interstellar Medium: The Cygnus Loop,” *Astrophys. J.* **178**, 143–157 (1972).
4. J. C. Raymond, “Shock Waves in the Interstellar Medium,” *Astrophys. J. Suppl. Ser.* **39**, 1–27 (1979).
5. V. I. Dokuchaev, “Self-Similar Spherical Shock Solution with Sustained Energy Injection,” *Astronaut. Astrophys.* **395**, p. 1023 (2006).
6. D. B. Geohegan, “Fast Intensified-CCD Photography of YBa<sub>2</sub>Cu<sub>3</sub>O<sub>7-x</sub> Laser Ablation in Vacuum and Ambient Oxygen,” *Appl. Phys. Lett.* **60** (22), 2732–2734 (1992).
7. S. H. Jeong, R. Greif, and R. E. Russo, “Propagation of the Shock Wave Generated from Excimer Laser Heating of Aluminum Targets in Comparison with Ideal Blast Wave Theory,” *Appl. Surf. Sci.* **127–129**, 1029–1034 (1998).
8. A. Misra and R. K. Thareja, “Investigation of Laser Ablated Plumes using Fast Photography,” *IEEE Trans. Plasma Sci.* **27** (6), 1553–1558 (1999).
9. P. Phelps, C. J. Druffner, G. P. Perram, and R. R. Biggers, “Shock Front Dynamics in the Pulsed Laser Deposition of YBa<sub>2</sub>Cu<sub>3</sub>O<sub>7-x</sub>,” *J. Phys., D: Appl. Phys.* **40** (15), 4447–4453 (2007).
10. L. I. Sedov, *Similarity and Dimensional Methods in Mechanics* (Izd. Tekh.-Teor. Lit, Moscow, 1957; Academic Press, New York, 1959).
11. G. I. Taylor, “The Formation of a Blast Wave by a Very Intense Explosion,” *Proc. Roy. Soc. A* **201**, 159–174 (1950).
12. Ya. B. Zel’dovich and Yu. P. Raizer, *Physics of Shock Waves and High-Temperature Hydrodynamic Phenomena* (GIFML, Moscow, 1955; Academic Press, New York, 1967).
13. G. A. Askar’yan, M. A. Rabinovich, M. M. Savchenko, et al., “Optical Breakdown of the Fireball in the Laser Beam Focus,” *Pis’mu Zh. Eksp. Teor. Fiz.*, No. 5, 150–154 (1967).

14. J. Wilkinson, J. M. Lightstone, C. J. Boswell, and J. R. Carney, "Emission Spectroscopy of Aluminum in Post-Detonation Combustion," *Shock Compression Cond. Matter* **955** (1), 1271–1274 (2007).
15. M. H. Keshavarz, H. Motamedoshariati, R. Moghayadnia, et al., "A New Computer Code to Evaluate Detonation Performance of High Explosives and Their Thermochemical Properties, Part I," *J. Hazard Mater.* **172** (2–3), 1218–1228 (2009).
16. G. D. Yngve, J. F. O'Brien, and J. K. Hodgins, "Animating Explosions," in *Proc. of the 27th Annu. Conf. on Computer Graphics and Interactive Techniques, SIGGRAPH'00* (2000), pp. 29–36.
17. A. N. Dills, S. C. Gustafson, and G. P. Perram, "Detonation Discrimination and Feature Saliency using a Near-Infrared Focal Plane Array and a Visible CCD Camera," *Proc. SPIE* **5811**, 123–132 (2005).
18. M. A. Cook, A. S. Filler, R. T. Keyes, et al., "Aluminized Explosives," *J. Phys. Chem.* **61** (2), 189–196 (1957).
19. M. F. Gogulya, A. Y. Dolgoborodov, and M. A. Brazhnikov, "Investigation of Shock and Detonation Waves by Optical Pyrometry," *Int. J. Impact Eng.* **23**, 283–293 (1999).
20. A. Lefrancois, G. Baudin, C. L. Gallic, et al., "Nanometric Aluminium Powder Influence on the Detonation Efficiency of Explosives," in *12th Symp. (Int.) on Detonation* (San Diego, 2002), p. 22.
21. P. Brousseau, H. E. Dorsett, M. D. Cliff, et al., "Detonation Properties of Explosives Containing Nanometric Aluminum Powder," in *12th Symp. (Int.) on Detonation* (San Diego, 2002), p. 11.
22. J. R. Carney, J. S. Miller, J. C. Gump, et al., "Atmospheric Effects on the Combustion of Detonating Aluminized Explosives," *Shock Compres. Cond. Matter* **845** (1), 948–951 (2006).
23. S. D. Gilev and V. F. Anisichkin, "Interaction of Aluminum with Detonation Products," *Fiz. Goreniy Vzryva* **42** (1), 120–129 (2006) [*Combust., Explos., Shock Waves* **42** (1), 107–115 (2006)].
24. J. R. Carney, J. S. Miller, J. C. Gump, et al., "Time-Resolved Optical Measurements of the Post-Detonation Combustion of Aluminized Explosives," *Rev. Sci. Instrum.* **77** (6), 063103-1–063103-6 (2006).
25. J. R. Carney, J. Wilkinson, and J. M. Lightstone, "Time-Resolved Optical Measurements of Detonation and Combustion Products," *Shock Compression Cond. Matter* **955** (1), 1225–1228 (2007).
26. J. M. Peuker, P. Lynch, H. Krier, et al., "Optical Depth Measurements of Fireballs from Aluminized High Explosives," *Opt. Lasers Eng.* **47** (9), 1009–1015 (2009).
27. P. W. Cooper, *Explosives Engineering* (VCH Publ., New York, 1996).
28. R. C. Gonzalez, R. E. Woods, and S. L. Eddins, *Digital Image Processing Using Matlab* (Pearson Prentice-Hall, Upper Saddle River, 2004).
29. C. Callies, P. Berger, and H. Hugel, "Time-Resolved Observation of Gas-Dynamic Discontinuities Arising during Excimer-Laser Ablation and Their Interpretation," *J. Phys., D: Appl. Phys.* **28**, 794–806 (1995).
30. A. Sakurai, "Blast Wave Theory," MRC Technical Summary Report No. 497 (Mathematics Research Center, United States Army, Univ. of Wisconsin, Madison, 1964).
31. W. E. Baker, *Explosions in Air* (Univ. of Texas Press, Austin, 1973).
32. C. E. Needham, *Blast Waves* (Springer-Verlag, Heidelberg, 2010).
33. G. E. Jamieson and G. C. Wetsel, Jr., "Optical-Beam-Deflection Probing of Blast Waves near Solid Surfaces," in *IEEE 1985 Ultrasonics Symp. Proc.* (1985), pp. 451–456.
34. T. Zyung, H. Kim, J. C. Postlewaite, et al., "Ultrafast Imaging of 0.532- $\mu\text{m}$  Laser Ablation of Polymers: Time Evolution of Surface Damage and Blast Wave Generation," *J. Appl. Phys.* **65** (12), 4548–4565 (1989).
35. J. Diaci and J. Možina, "Investigation of Blast Waves Generated by Laser Induced Damage Processes," *Opt. Commun.* **90** (1–3), 73–78 (1992).
36. S. J. Lee, K. Imen, and S. D. Allen, "Shock Wave Analysis of Laser Assisted Particle Removal," *J. Appl. Phys.* **74** (12), 7044–7049 (1993).
37. J. G. Anderson, G. Katselis, and C. Caputo, "Analysis of a Generic Warhead. Part I: Experimental and Computational Assessment of Free Field Overpressure," *DSTOTR-1313—Australian Defence Science and Technology Organisation* (Systems and Sciences Laboratory, Edinburgh, 2002).
38. J. M. Gordon, "Shock Wave Dynamics of Novel Aluminized Detonations and Empirical Model for Temperature Evolution from Post-Detonation Combustion Fireballs," Ph.D. Dissertation AFIT/DS-ENP/10-S03 (Dept. of Eng. Phys., Air Force Inst. of Technology, 2011).
39. M. T. Spidell, J. M. Gordon, J. Pitz, et al., "High Speed Radiometric Measurements of IED Detonation Fireballs," *Proc. SPIE* **7668**, 76680C-1–76680C-10 (2010).